Scilight

Bulletin of Computational Intelligence
https://www.sciltp.com/journals/bci

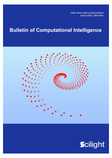

Article

Optimized Noise Suppression of Acceleration Records from Shaking-Table Tests Using Signal Processing and Deep Learning Techniques

Leonidas Alexandros S. Kouris [1,2,3,*,†], Andrea Penna [2,3] and Guido Magenes [2,3]

[1] Institute for Advanced Studies, IUSS Pavia, p. della Vittoria 15, 27100 Pavia, Italy
[2] DICAr, University of Pavia, v. Ferrata 3, 27100 Pavia, Italy
[3] European Centre for Training and Research in Earthquake Engineering, v. Ferrata 1, 27100 Pavia, Italy
* Correspondence: leonidasalexandros.kouris@unipv.it
† Current Address: Joint Research Centre, European Commission, Via Enrico Fermi 2749, 21027 Ispra, Italy.

How To Cite: Kouris, L.A.S.; Penna, A.; Magenes, G. Optimized Noise Suppression of Acceleration Records from Shaking-Table Tests Using Signal Processing and Deep Learning Techniques. *Bulletin of Computational Intelligence* **2026**, *2*(2), 164–180. https://doi.org/10.53941/bci.2026.100009

Received: 7 March 2026
Revised: 15 April 2026
Accepted: 21 April 2026
Published: 8 May 2026

Abstract: Reliable displacement reconstruction from acceleration measurements is a persistent challenge in shaking-table testing because sensor noise and baseline drift can accumulate through numerical integration, biasing the inferred kinematic response. This study investigates and compares two complementary strategies for noise suppression and displacement estimation: (i) an optimized signal-processing workflow that combines band-limited integration with systematic parameter tuning, and (ii) a data-driven approach based on a Long Short-Term Memory (LSTM) neural network trained to map acceleration time histories to displacement. For the signal-processing workflow, filter parameters are selected through a multi-objective search using Latin Hypercube Sampling (LHS) to minimize reconstruction error against reference displacement measurements while limiting drift and spurious low-frequency content. For the LSTM approach, model hyperparameters are selected via Bayesian optimization to balance accuracy and generalization across excitation phases. The methods are assessed on shaking-table records from an instrumented experimental campaign, using displacement transducers as reference. Results indicate that both approaches substantially reduce integration drift and noise-induced artefacts compared with conventional fixed filtering and detrending. The optimized signal-processing pipeline provides a transparent, physically interpretable baseline with strong accuracy, whereas the LSTM model can achieve comparable performance with reduced need for manual tuning and improved robustness to non-stationary noise characteristics. The proposed framework offers a reproducible benchmark for computational-intelligence methods in vibration data post-processing and supports more reliable displacement estimation in experimental structural dynamics.

Keywords: structural displacement reconstruction; shaking-table testing; non-causal filtering; adaptive filtering; deep learning

1. Introduction

In earthquake engineering shaking table tests are an essential tool for assessing the behavior of structures. Shaking-table tests which already date back nearly a century ago [1] are performed to assess the seismic performance of structures to earthquake shaking. Given the substantial cost associated with full-scale experiments only a few specimens can be tested subjected to a limited number of accelerograms to assess their linear and nonlinear response up to failure. Consequently, inherently stochastic seismic phenomena are represented using a finite number of deterministic excitation records, which introduces uncertainty in the interpretation of structural performance.

In addition, the large volume of data generated during shaking-table experiments requires systematic and rigorous processing to extract meaningful conclusions. Despite advances in sensing technology and instrumentation, experimental measurements remain affected by various sources of noise and systematic errors. One of the fundamental challenges in signal recording is the effective suppression of noise while preserving the true structural response.

Acceleration measurements obtained during shaking-table tests are particularly susceptible to noise. There is a variety of external sources of noise in acceleration measurements during shaking table tests such as adjacent electrical and mechanical equipment, vehicle traffic etc. [2]. Land seismic measurements suffer from noise [3,4] as well and similar processing techniques are applied.

Structural displacements are typically obtained through double integration of measured accelerations e.g., [5,6]. However, high-frequency noise or low-frequency drift is quadratically amplified during integration, leading to severe distortions in the reconstructed displacement traces. Hence, robust and optimized denoising methodologies are required to ensure reliable displacement reconstruction.

Conventional methodologies rely on signal processing techniques e.g., [7]. More recently, machine learning (ML) and deep learning (DL) methods have been proposed e.g., [8–11]. In fact, ML has been applied to several disciplines of structural analysis and testing generating accurate predictions [12–16].

Measurement errors are generally classified in two broad categories: (a) systematic errors which consistently bias every measurement and depend on the accuracy of the detectors, and (b) random errors which introduce stochastic interference into measurements. While ensemble averaging—the averaging of repeated experimental trials—is a common statistical approach [17,18], it is impossible for real seismic events or destructive laboratory tests where exact repetitions are impossible.

This study investigates and compares the effectiveness of several displacement reconstruction methodologies based on recorded acceleration signals:

- Non-causal (NC) filtering where noise is isolated within the frequency domain within an optimization framework;
- Adaptive filtering, utilizing auxiliary displacement transducer measurements to optimize filter coefficients in real-time;
- Data-driven modeling, employing deep neural networks trained to map noisy acceleration records directly to displacement time-histories.

NC methods utilize the full time-history of the seismic event and can be more accurate in reconstructing displacement traces while causal methods are essential for real-time structural health monitoring. The transition from linear-elastic to nonlinear-damaged states in masonry involves significant spectral non-stationarity. In the frequency domain, this is characterized by a downward shift in the fundamental frequency and the emergence of higher-order harmonics. While the NC filter employs a global optimization of the transfer function, its performance is inherently capped by the assumption of a stationary system. Time-domain recurrent models, however, maintain the capacity to adapt to these evolving structural properties, providing a potential advantage in monitoring structures undergoing active damage evolution.

2. Shaking Table Tests of an Unreinforced Stone Masonry Building and Definitions

2.1. Test Description

For completeness, a brief description of the experimental program is provided in this section. A full-scale two-storey UnReinforced Stone Masonry (URSM) building was tested on a shaking table at the EUCENTRE laboratory in Pavia, Italy [19] to investigate the nonlinear behavior and the failure mechanism of existing URSM structures. A sequence of tests with a progressively increasing seismic intensity was performed (Figure 1).

The two-story building is 4.70 m by 6.60 m in plan and is 6 m high. A double-pitch timber roof with 1 m high gable roof covers the structure. The excitation is unidirectional along the longitudinal axis of the building corresponding to the ridge beam of the roof direction. The building has stiffness eccentricity in both directions due to asymmetric openings in both principal directions (Figure 1). Details regarding the geometry and the structural characteristics of the specimen are in [20] while a twin strengthened structure was tested later [21].

The unreinforced building was subjected to five dynamic tests with increasing seismic excitation in the long direction (nominal PGAs = 0.05 g, 0.10 g, 0.20 g, 0.30 g and 0.40 g and see Figure 1). The excitation is the scaled versions of the accelerogram recorded during the M_w 6.9 Montenegro Earthquake 1979 (Ulcjni-Albatros hotel record) to predefined values of peak acceleration. The building exhibited gradually increasing damage while during the fifth test, a near out-of-plane collapse [22]. Each dynamic test on the shaking table was preceded by some calibration tests of random vibrations (stationary processes). Figure 1 presents the sequence of the base acceleration used in these tests.

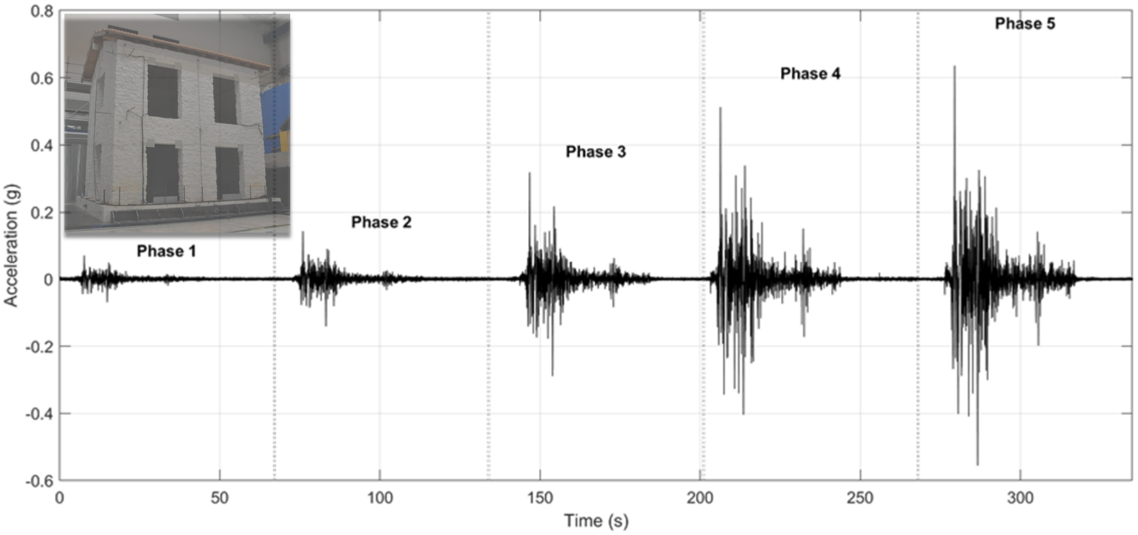

Figure 1. The sequence of seismic inputs of the building specimen on the shake table.

Prior to each seismic test, calibration tests involving stationary random vibrations were performed to assess the dynamic properties of the structure. Modal frequencies of the structure vary between 5 and 40 Hz for all test phases [23,24].

2.2. Instrumentation

Detection and monitoring of the structural response was performed using two types of sensors placed on the building: (i) force feedback capacitive accelerometers for acceleration measurement, and (ii) potentiometers and displacement transducers for displacement measurement. The location of each type was designed to capture the response of the critical zones of the building (Figure 2).

The accelerometers have an acceleration bandwidth of ±2.5 g, a resolution (i.e., the smallest detectable increment in acceleration) of 0.8 μg at least when the frequency is 1 Hz, a nominal resonant frequency equal to 5000 Hz and a weight of 28 g. Accelerometers have been placed on the structures to measure the response of the buildings in all the three directions *x*, *y* and *z*, with *x* being the direction of application of the input motion from the uniaxial shaking table.

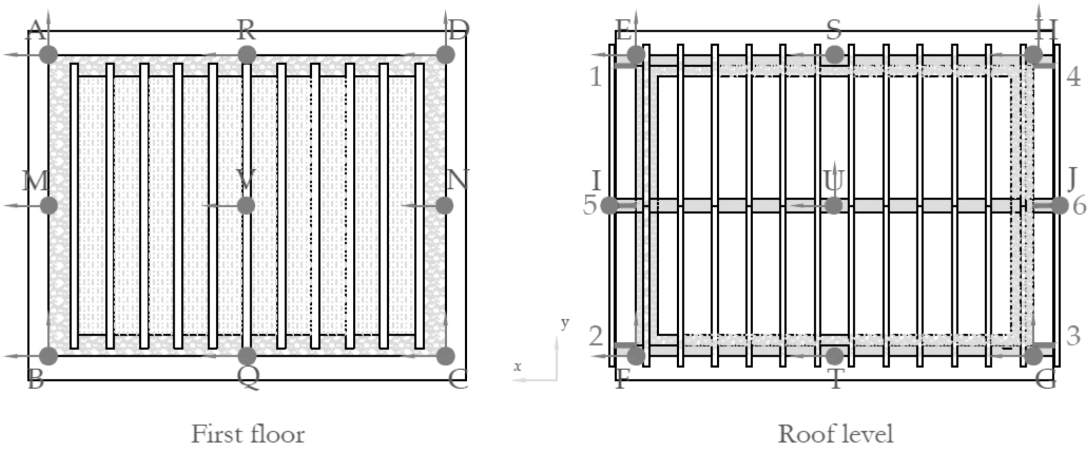

Figure 2. Plan view of the location of capacitive accelerometers (grey bullets) on the critical zones of the building.

Eighteen accelerometers were placed at the first storey and the roof level, as shown in Figure 2. Two single channel accelerometers were located at the base of the structure (i.e., shaking table level) and two at the middle of the base of the gables, resulting in a total of 22 acceleration channels recorded (Figure 2). Moreover, a linear displacement transducer with ball tip and a cylindrical case was used, to detect the relative displacements of the shaking table. The latter measurements, that is the displacement recordings of the transducer at the base together with the two recordings from the accelerometers on the shaking table provide a set where a comparison of displacements from double integration and measured displacement is possible. However, it should be noted that the cross-correlation between the recordings of the two accelerometers on the seismic table is around 95% indicating a slight tilt of the table.

2.3. Definitions

Noise can be defined as any undesired signal intruding on the waveform. Noise can obscure spectral data, alter amplitude information and render measurements useless. When integrated, noise is amplified leading to significant drift and distortion in the reconstructed displacement time histories.

Let $\ddot{x}_i(n)$ denote the acceleration measurement at a point *i* of the structure and at a discrete time *n* while, *x(n)* the respective displacement measurement at the base. The sampling frequency F_s of the accelerometers and the displacement transducer is 0.96 kHz. The sampling frequency of 0.96 kHz was employed, providing an oversampling ratio of 24 relative to the primary modal frequencies (expected in the range 5–40 Hz). This configuration ensures sufficient temporal density for accurate peak detection while moving the Nyquist limit to 480 Hz, thereby preventing aliasing of high-frequency electrical or ambient noise into the structural frequency band.

The acceleration measurement $\ddot{x}_i(n)$ is affected by noise. Sensor bias represents a primary source of uncertainty in MEMS (Micro Electro Mechanical Systems) acceleration monitoring, as the double integration of a DC (direct current) offset results in quadratic displacement drift. To mitigate this, the optimized non-causal high-pass filter and the recurrent states of the Bi-LSTM are utilized to decouple the low-frequency sensor artifacts from the true structural vibrations, ensuring that the reconstructed displacement remains physically bounded and centered on the zero-baseline. Let signals $\ddot{u}_i(n)$ represent the true (unknown) acceleration response. Hence, the objective of the filtering process of the accelerations $\ddot{x}_i(n)$ is to specify the coefficients of a filter such that the filtered output $\tilde{\ddot{u}}_i(n)$ will be the same as the true acceleration $\ddot{u}_i(n)$ [25]. In general, this is partially achievable and the difference between these two is the error denoted as *e*(n), i.e.,

$$e(n) = \tilde{\ddot{u}}_i(n) - \ddot{u}_i(n) \tag{1}$$

Equation (1) highlights that the filtering process is an optimisation process to reduce error. Although, $\ddot{u}_i(n)$ is not generally known, the displacement transducer measures the displacement of the table and in this case, can be used as a benchmark.

To estimate the performance of the filtering process we employ Equation (1) and the following three evaluation metrics:

i. The Pearson correlation index (R) to measure apart from shape similarity, phase lag.
ii. The root mean square error (RMSE) which provides the standard deviation of *e*(n).
iii. The peak-to-peak error (ε_{peak}) which is the percentage difference between the maximum displacement recorded by the LVDT and the estimated one according to Equation (2)

$$\varepsilon_{peak} = \frac{|u_{max} - \tilde{u}_{max}|}{u_{max}} \times 100\% \tag{2}$$

Moreover, for the physics-based procedure where filters are applied to denoise recorded accelerations, the ratio of the corresponding powers of the original and the filtered signals is the signal-to-noise ratio (SNR) (Equation (3)). SNR is an indication of the amount of cancelled noise expressed usually in a logarithmic scale (dB).

$$SNR = \frac{\text{Average signal power}}{\text{noise power}} = 20\log_{10}\left(\frac{\sum x_n^2}{\sum e^2}\right) \tag{3}$$

The procedure to retrieve the displacement time-histories $u_i(t)$ from the acceleration time-histories $\ddot{u}_i(t)$ is based on the double integration of the latter. This integration is performed in the time domain. The accumulation of error by integration leads to total deviation from the real displacements with large permanent drifts [26] due to linear and quadratic errors [27]. An alternative may be the integration in the frequency domain [28]. The equations of the integration are as follows:

$$M\ddot{u} + C\dot{u} + Ku = f \tag{4a}$$

$$\dot{u}_i(t) = \int_{t_0}^{T} \ddot{u}_i(t)\,dt + \dot{u}_i(t_0) \tag{4b}$$

$$u_i(t) = \int_{t_0}^{T} \dot{u}_i(t)\, dt + u_i(t_0) \tag{4c}$$

where in Equation (4a) $\ddot{u}$, $\dot{u}$ and u denote the vectors of accelerations, velocities and displacements respectively and f the restoring force in time t and M, C, K the mass, damping and stiffness matrices of the structure.

3. Optimized Double Integration of Acceleration Filtered in the Frequency Domain

An ideal band-pass filter (BPF) has a rectangular frequency response that perfectly attenuates frequencies above the cut-off thresholds (i.e., the high pass frequency ω_{hp} and low pass frequency ω_{lp}) while allowing lower frequencies to pass unaffected as shown in Equation (5).

$$H(\omega) = \begin{cases} 1\, for\ \omega_{hp} < \omega < \omega_{lp} \\ 0\, for\ \omega < \omega_{hp}\ or\ \omega > \omega_{lp} \end{cases} \tag{5}$$

In practice, ideal filters cannot be implemented in real time because their impulse response extends infinitely in both forward and backward time directions, making them inherently non-causal. However, non-causal (NC) filters are applicable in post-processing applications, where the complete signal time history is available. It should be noted that truncating the impulse response leads to Gibbs phenomenon (oscillatory artifacts) unless appropriate windowing is applied. To minimize spectral leakage and the resulting potential for artificial low-frequency drift, a hanning-tapered windowing function was applied to the seismic phases. This preprocessing step ensures the stability of the NC optimum filter by concentrating the signal energy within the structural modal bands, thereby preventing the 'smearing' of spectral components that could otherwise compromise the accuracy of peak displacement retrieval.

In the context of shaking table tests, however, these constraints can be mitigated. Post-processing allows for NC filtering, where the entire measurement history is available. By utilizing a pre-event buffer (baseline recording) and the full recorded duration, NC filter can account for both 'past' and 'future' samples relative to any given time step (n), effectively minimizing transient distortions. Thus, NC filter is applicable with a maximum degree of accuracy [29,30].

The optimization of the NC filter cut-off frequencies (ω_{hp} and ω_{lp}) was performed using a Latin Hypercube Sampling (LHS) strategy to ensure a statistically robust exploration of the parameter space. Unlike traditional random sampling, LHS partitions each parameter's probability distribution into N intervals of equal probability and selects one sample from each interval. This ensures effective representation of the entire range of potential cut-off frequencies without the computational expense of Monte Carlo methods [31].

In this study, 200 realizations were generated within the search bounds $\omega_{hp} = 2\pi \times [0.01, 0.15]$ Hz and $\omega_{lp} = 2\pi \times [30, 60]$ Hz for the low-pass filter. The samples were transformed using an inverse cumulative distribution function (ICDF) to follow a normal distribution centered within the bounds (Figure 3). The robustness of the LHS strategy was verified through a sensitivity analysis, which confirmed that $N = 200$ realizations were sufficient to reach a stable convergence of the cost function. By mapping the LHS intervals through a Gaussian ICDF, the search was prioritized toward the central regions of the frequency bounds—aligning with expected structural modal characteristics—while preserving the ability to explore edge-case scenarios that uniform sampling might over-represent or miss entirely.

Each sample was evaluated against a multi-objective cost function comprising the evaluation metrics: Pearson correlation (R), Root Mean Square Error (RMSE), Peak-to-Peak error (ε_{peak}), and Signal-to-Noise Ratio (SNR). Specific weights w were assigned to cost parameters to increase the fidelity of the retrieved displacements: $w_R = 1$, $w_{RMSE} = 0.5$, $w_{\varepsilon p} = 1$, $w_{SNR} = 0.2$ (Equation (5)). The optimum frequency pair for each test phase was then identified as the realization that minimized the global residual between the reconstructed analytical displacement and the measured LVDT ground truth (Figure 4). The results of the optimization process are presented in Figure 4.

$$cost = w_R(1 - R) + w_{RMSE}(100 \cdot RMSE) + w_{\varepsilon p}\varepsilon_p + {}^{w_{SNR}}/_{SNR} \tag{6}$$

The cost function weights were adopted to emphasize structural response characteristics over global statistical errors. By assigning unit weights to w_R and $w_{\varepsilon p}$, the optimization process prioritized temporal synchronization and peak displacement accuracy both vital for masonry damage detection. RMSE was assigned a moderate weight to maintain overall waveform fidelity without over-penalizing baseline noise while a lower weight for SNR ensured that signal-to-noise refinement did not compromise the reconstruction of high-amplitude transient peaks. NC filtering was applied with the optimized cut-off frequencies (ω_{hp} and ω_{lp}) shown in Table 1 to the recorded accelerations and then, displacements are obtained by a double integration as per Equations (4).

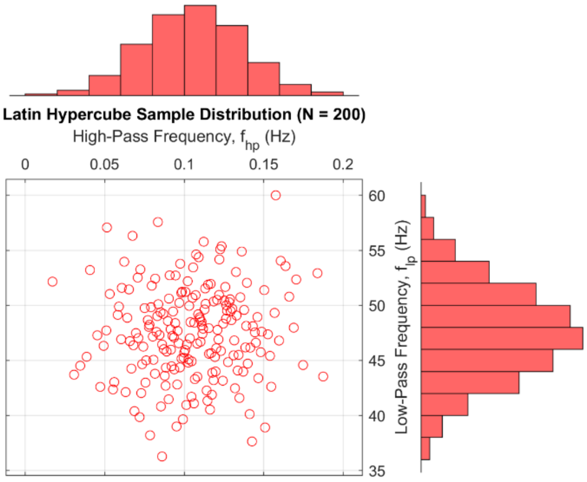

Figure 3. Cut-off frequencies ω_{hp} and ω_{lp} samples using LHS.

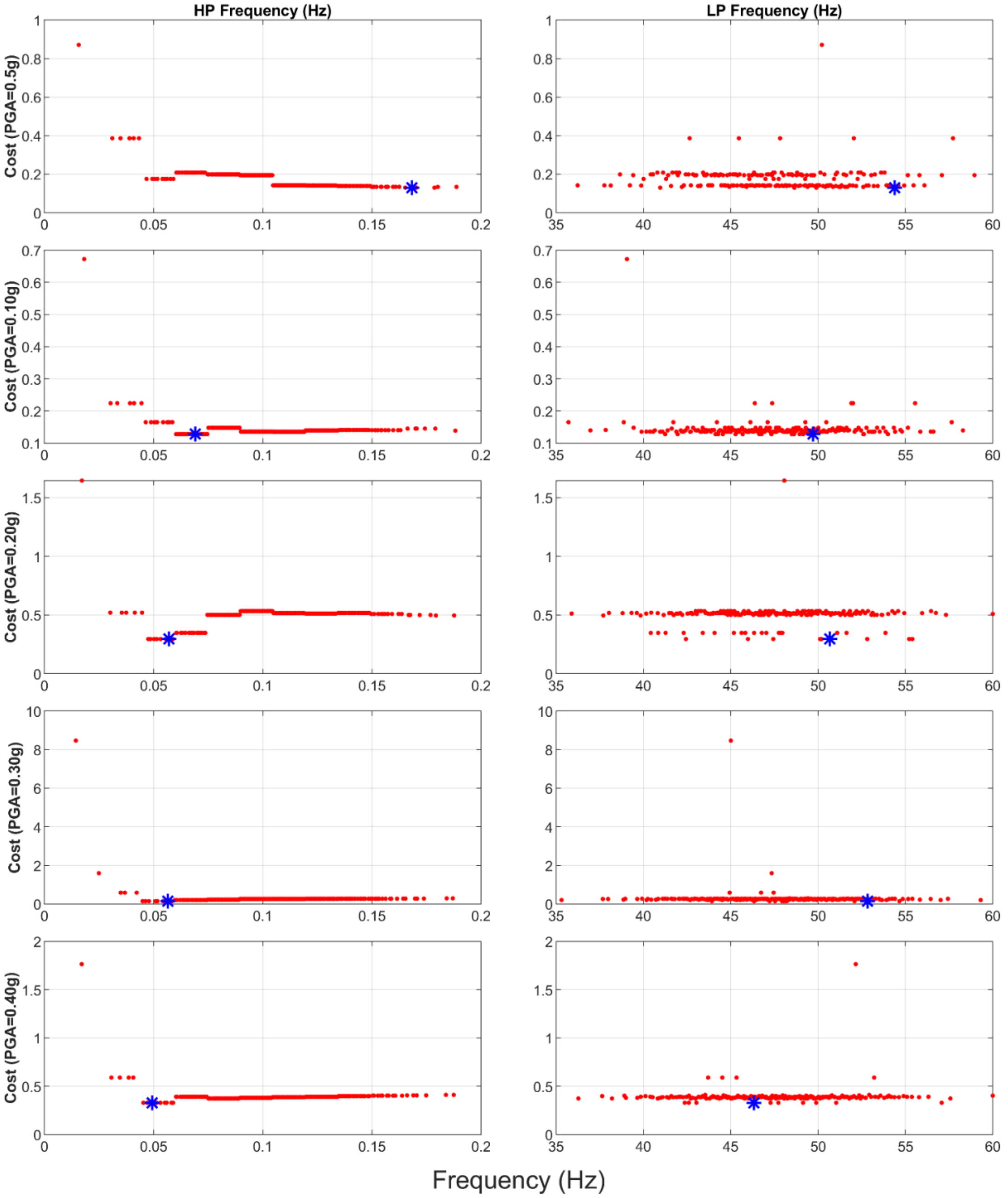

Figure 4. Parameter optimisation applying weighted cost across test phases for cut-off (HP and LP) frequencies.

The achieved ratio of the peak values ε_{peak} between the analytically derived and measured displacements is less than 5% in all cases (Table 1). SNR varies between 10 dB for the third test phase and 17 dB for the fourth phase. The integration of the acceleration time-histories (Figure 5) shows a close agreement with the measured displacement time-history is on average 94% varying from 87% or the worst case to 98% for the fourth test phase. The peak-to-peak error is small (5.7% on average). It is interesting to note that the noise time history has a shape close to Additive White Gaussian (AWG) noise and the baseline detrending is almost linear.

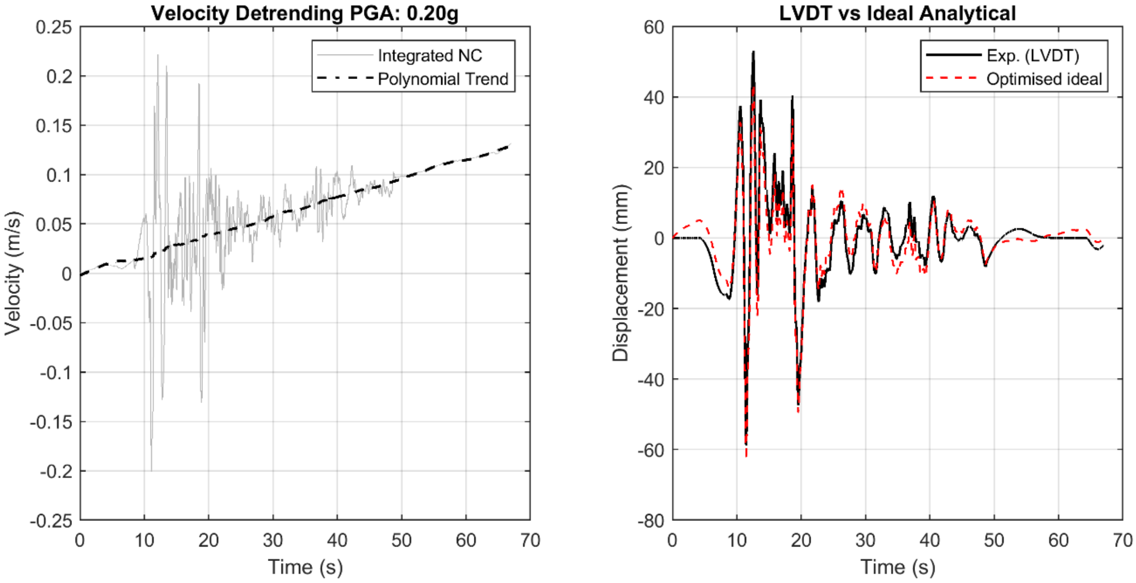

Figure 5. Comparison of the actual displacement and the analytically derived time-histories after NC filtering for test phase 3 at nominal PGA = 0.20 g: (**a**) linear trend in the integrated acceleration time-history, (**b**) displacement time-histories.

Table 1. Optimised cut-off frequencies and evaluation metrics for ideal filter.

PGA (g%)	$\omega_{c,high\ pass}$ (Hz)	$\omega_{c,low\ pass}$ (Hz)	Correlation (R)	RMSE (mm)	ε_{peak} (%)	SNR (dB)
5	0.17	54	0.96	0.01	3.8	11.1
10	0.06	50	0.97	1.24	2.1	12.4
20	0.06	51	0.95	3.53	5.0	10.2
30	0.05	53	0.99	2.14	1.9	17.0
40	0.05	46	0.97	5.46	1.4	12.2

4. Hybrid Double Integration of Acceleration Filtered in Time Domain

Noise $e(n)$ is formed by subtracting the true acceleration signal $\ddot{u}(n)$ from the filtered signal $\bar{\ddot{u}}(n)$ (Equation (1)). Adaptive filtering $W(z)$ provides an alternative signal reconstruction framework by dynamically adjusting filter coefficients to minimize reconstruction error. Unlike fixed filters, adaptive filters exploit statistical relationships between noisy measurements and reference signals to achieve optimal noise suppression. To address the non-stationary nature of seismic records, the Wiener filter was adapted into NC optimum framework. This adaptation facilitates a zero-phase frequency-response function that utilizes the total signal energy to distinguish structural vibrations from sensor-induced noise. By performing the optimization over the entire time-history, the NC filter achieves a stable reconstruction that is immune to the transient instabilities and phase lags typically associated with real-time, causal filtering techniques.

Several methods have been proposed to implement the optimal filter in the past and recently e.g., [32–36] and among them the normalized least mean square (NLMS) algorithm [37].

In the latter, the optimality condition is achieved by minimizing the error ε which in a mean-square sense is determined as the expected value of $e^2(n)$ denoted as $\mathrm{E}\{|e(n)|^2\}$. Hence, the condition for error ε is as follows:

$$\varepsilon = \min(E\{|e(n)|^2\}) = \min(E\{|\ddot{u}(n) - \bar{\ddot{u}}(n)|^2\}) \tag{7}$$

The structure of this adaptive method is presented in Figure 6 where the input to the adaptive filter is the noisy acceleration $\ddot{x}(n)$ and the output would be the displacements $\bar{\ddot{u}}(n)$. The transfer function $H(z)$ refers to the system $W(z)$ with the best correlations. The filtered accelerations $\ddot{u}_n$ are those using the optimized NC filter.

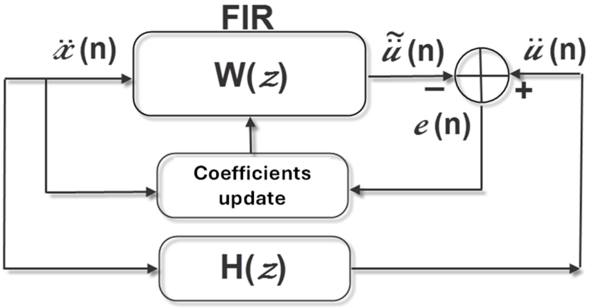

Figure 6. The structure of the adaptive filter.

The output signal $\bar{\ddot{u}}_n$ is:

$$\tilde{\ddot{u}}(n) = \sum_{k=0}^{N-1} w(k) \cdot \ddot{x}(n-k) \tag{8}$$

where *w(n)* is the impulse response of the system as follows:

$$\ddot{\mathbf{x}}(\mathbf{n}) = \begin{bmatrix} x(n) \\ x(n-1) \\ \vdots \\ x(n-N+1) \end{bmatrix}, \mathbf{w} = \begin{bmatrix} w(0) \\ w(1) \\ \vdots \\ w(N-1) \end{bmatrix} \tag{9}$$

Equation (8) is then written:

$$\bar{\ddot{u}}(n) = \mathbf{w}^{\mathrm{T}}\ddot{\mathbf{x}}(\mathbf{n}) = \ddot{\mathbf{x}}(\mathbf{n})^{\mathrm{T}}\mathbf{w} \tag{10}$$

The mean-square error ε defined in Equation (7) is derived using vector notation:

$$\begin{gathered} \varepsilon = \mathrm{E}\{|e(n)|^2\} = \mathrm{E}\{|\ddot{u}(n) - \bar{\ddot{u}}(n)|^2\} = \mathrm{E}\{[\ddot{u}(n) - \mathbf{w}^{\mathrm{T}}\ddot{\mathbf{x}}(\mathbf{n})]^2\} \\ \varepsilon = \mathrm{E}\{\ddot{u}^2(n) - 2 \cdot \ddot{u}(n) \cdot \ddot{\mathbf{x}}(\mathbf{n})^{\mathrm{T}}\mathbf{w} + \mathbf{w}^{\mathrm{T}}\ddot{\mathbf{x}}(\mathbf{n}) \cdot \ddot{\mathbf{x}}(\mathbf{n})^{\mathrm{T}}\mathbf{w}\} \end{gathered} \tag{11}$$

$$\varepsilon = \mathrm{E}\{\ddot{u}^2(n)\} - 2 \cdot \mathrm{E}\{\ddot{u}(n) \cdot \ddot{\mathbf{x}}(\mathbf{n})^{\mathrm{T}}\} \cdot \mathbf{h} + \mathbf{w}^{\mathrm{T}} \cdot \mathrm{E}\{\ddot{\mathbf{x}}(\mathbf{n}) \cdot \ddot{\mathbf{x}}(\mathbf{n})^{\mathrm{T}}\} \cdot \mathbf{w} \tag{12}$$

In Equation (12) the first term is a scalar value denoted as K_u. The second term is a cross-correlation vector between the desired acceleration signal $\ddot{u}(n)$ and the noisy measurement $\ddot{x}(n)$ denoted as r_{ux}. The third term is the expected value of an autocorrelation matrix of the noisy measurement $\ddot{x}(n)$ denoted as R_x. Therefore, the following definitions apply:

$$\begin{gathered} \mathrm{K_u} = \mathrm{E}\{\ddot{u}^2(n)\} \\ \mathbf{r_{ux}} = \mathrm{E}\{\ddot{u}(n) \cdot \ddot{\mathbf{x}}(\mathbf{n})^{\mathrm{T}}\} \\ \mathbf{R_x} = \mathrm{E}\{\ddot{\mathbf{x}}(\mathbf{n}) \cdot \ddot{\mathbf{x}}(\mathbf{n})^{\mathrm{T}}\} \end{gathered} \tag{13}$$

Substituting Equation (13) to the error in Equation (12) yields:

$$\varepsilon = \mathrm{K_u} - 2 \cdot \mathbf{r_{ux}}^{\mathrm{T}} \cdot \mathbf{w} + \mathbf{w}^{\mathrm{T}}\mathbf{R_x}\mathbf{w} \tag{14}$$

The minimum error results from its derivative with respect to the impulse coefficients $w(k)$ which is set equal to zero:

$$\frac{\partial \varepsilon}{\partial w(k)} = \frac{\partial}{\partial w(k)} E\{e^2(n)\} = -2 \cdot \mathbf{r_{ux}}^{\mathrm{T}} + 2 \cdot \mathbf{R_x}\mathbf{w} = 0 \tag{15}$$

Equation (15) solved for **w** yields to:

$$\mathbf{w} = \mathbf{R_x}^{-1} \cdot \mathbf{r_{ux}} \tag{16}$$

The above equation determines the optimal Wiener-Hopf filter coefficients in a mean-square statistical sense. The adaptive filter coefficients were derived by solving Equation (16) in the time domain. By utilizing the cross-correlation between the raw experimental data and an LHS-optimized target signal, the filter order (*p*) was utilized to construct a Toeplitz auto-correlation matrix. The inversion of this matrix yields the optimal impulse response required to stabilize the acceleration record against non-stationary noise. Hence, the implementation of the adaptive Wiener filter in the time domain to ensure numerical stability and avoid spectral artifacts consists of:

1. Reference Generation: Constructing a target displacement signal via an LHS-optimized ideal band-pass filter (Section 3).
2. Statistical Characterization: Computing the auto-correlation $\mathbf{R}_{\mathbf{x}}$ and cross-correlation $\mathbf{r}_{\mathbf{ux}}$ (Equation (13)) of the signals (filtered and unfiltered) to populate a Toeplitz system matrix.
3. Coefficient Optimization: Solving the Wiener-Hopf equations through direct matrix inversion to identify the optimal FIR filter weights (w) in Equation (16).
4. Phase-Adaptive Mapping: Repeating the optimization for each seismic intensity phase to account for evolving structural dynamics and varying noise floors.

The integration of acceleration time-histories is applied as in the case of the frequency domain filters and the results are presented in Table 2. The comparison for the third phase between the analytically derived displacement time-histories after adaptive filtering and the actual one is presented in Figure 7 showing a high correlation 96%. In general, the correlation is slightly better than the optimized filter. It is also interesting to note that baseline trend during the first acceleration integration is absolutely linear as shown in Figure 7.

Table 2. Evaluation metrics for adaptive filter.

PGA (g%)	Correlation (R)	RMSE (mm)	ε_{peak} (%)	SNR (dB)
5	0.96	0.74	3.3	10.7
10	0.97	1.27	3.4	12.2
20	0.96	3.31	3.7	10.7
30	0.99	2.53	3.8	15.6
40	0.97	6.14	2.4	11.1

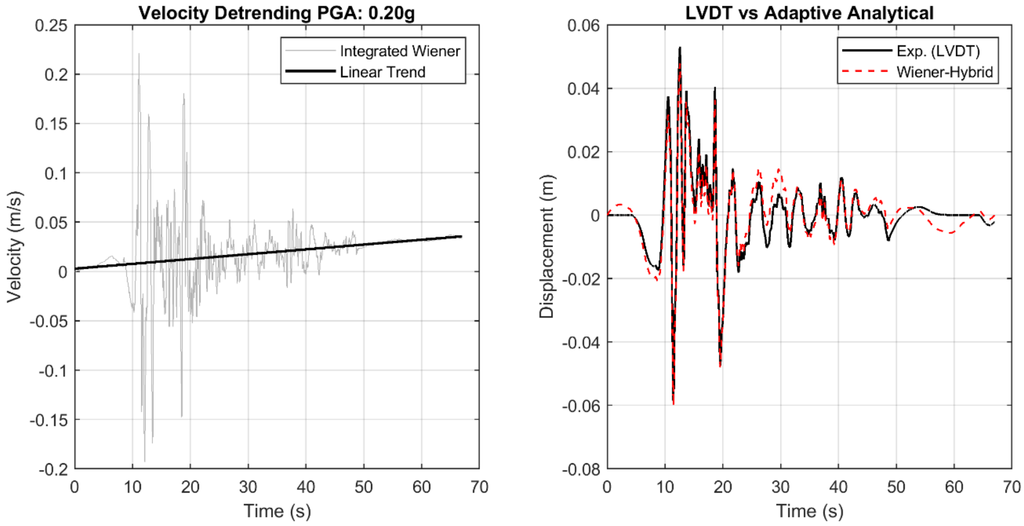

Figure 7. Comparison of the recorded displacement (LVDT) and the analytically derived after adaptive filtering time-histories.

5. Data driven Mapping Using Deep Learning

5.1. Direct Mapping to Displacements

Deep learning provides an alternative approach for noise suppression [25,38,39] and can be employed for displacement reconstruction by learning the implicit relationship between acceleration and displacement directly from data. In this study, a recurrent neural network (RNN) architecture with long short-term memory (LSTM) units was employed due to its ability to capture long-term temporal dependencies.

The reconstruction of displacement from acceleration is treated as an inverse problem. To overcome the ill-posed nature of discrete double integration (Equation (4)), the Bi-LSTM architecture functions as a learned regularizer. By optimizing the loss function, the problem is framed as a maximum likelihood estimation (MLE) over the total time steps N under the assumption of Gaussian noise:

$$\min_{\theta} \mathcal{L}(\theta) = \frac{1}{N}\sum_{i=1}^{N}\left(u_{LVDT} - \mathcal{F}(\ddot{u};\theta)\right)^2 \tag{17}$$

where u_{LVDT} denotes the reference displacement and θ the trainable parameters of the Bi-LSTM layers. The sampling time step ($\Delta t = 0.00104$ s) ensures numerical stability for the recurrent state updates within the Bi-LSTM architecture. The network incorporates prior knowledge of acceleration response that stabilize the inversion against sensor-induced noise and quadratic integration drift, whereas R, ε_p and SNR were not used for evaluation because MSE (mean squared error) sufficiently captured the physics of the displacements.

The proposed network consists of a stacked bidirectional LSTM (BiLSTM) architecture followed by fully connected regression layers. The network receives normalized acceleration time histories as input and produces displacement time histories as output.

The architecture of RNN includes an input normalization layer, fully connected (FC) layers with long-short term memory units accompanied by two dense layers in the decoder to output the displacement time-history. The bidirectional structure allows the network to learn both forward and backward temporal dependencies, improving reconstruction accuracy and stability.

Hyperparameters were optimized using Bayesian optimization with a Gaussian process surrogate model. The optimization variables included: (i) width of the FC layers, (ii) Learning rate (LR), (iii) L2 regularization coefficient, and (iv) Dropout ratio (DR). Five structures are compared with 128 or 256 LSTM units (U) and one or, two layers (L). Results are summarized in Table 3; comparing 128 U/1 L (loss = 0.1904) vs. 128 U/2 L (loss = 0.1789) proves that for seismic displacement data, adding a second layer is more effective than doubling the number of units in a single layer. Therefore, the two-layers of 128 LSTM units (128 U/2 L) appear to generalize well while achieving reasonable computational times when using a standard CPU power (i7 processor with 8 cores and 12 threads). On the other hand, a wider first layer increases the accuracy of the output albeit at computational cost. To get as reliable as possible predictions we opted for the 2 L architecture with 256 U and 128 U for the first and the second layers as shown in Figure 8.

Table 3. Optimization of the architecture; comparison between number of layers (L) and number of units (U).

Architecture	Best Validation Loss	Analysis Duration in Min @Epoch 100	Result
128 U/1 L	0.1904	45 min	Fast and stable but below accuracy limits.
128 U/2 L	0.1789	142 min	Accurate and fast.
256 U/1 L	0.1884	94 min	Wide but shallow.
256 U-128 U/2 L	0.1675	496 min	Most accurate.
256 U/2 L	0.1975	718 min	Very high cost for no accuracy gain.

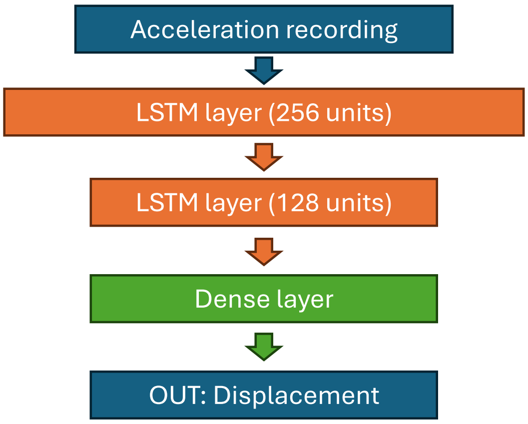

Figure 8. The architecture of the RNN with LSTM units.

The Bayesian optimization is then performed with twenty realizations. The optimization converged to an optimal rate near LR = 0.0005 achieving a validation root mean square error (RMSE) of 0.4957; beyond this threshold, the recursive nature of the double-integration mapping led to numerical instability (gradient explosion) due to the high-amplitude seismic record. The DR was estimated 0.2 and L2 is 0.001.

We used the recordings from four test-phases to train the data and one to validate them; to ensure rigorous model validation and prevent data leakage, a record-level partitioning strategy was adopted entirely excluding phase 0.20 g from the training dataset. This isolation ensures that the model's predictive capability is validated against a completely unseen structural response, while the use of localized record-specific normalization further guarantees that no global statistical properties were leaked during the optimization process. We selected the intermediate test phase 3 as during this phase the collapse mechanism initiated for the first time. Therefore, the structural performance is in between the elastic of the first two phases and the highly nonlinear of the two last phases. Given that the sampling frequency is constant across test phases, the validation set (phase 3) provides a statistical population of samples approximately equal to 20% of the total samples, ensuring that the performance metrics reflect the model's reliability across varying vibrational amplitudes and structural states.

We applied batches of 2 s (i.e., 2 × 960 time samples) and 0.5 s of overlapping between batches. Given that each test consists of 60,000 timesteps approximately, the Bi-LSTM training was conducted on a dataset comprising 60,000 × 4 acceleration-displacement pairs while the validation on 60,000 samples. Prior to training, the data underwent feature scaling to a [0, 1] range to optimize the activation of the LSTM gates. Scaling parameters were derived solely from the training distribution to avoid data leakage. The resulting dataset was partitioned into sequences using a look-back window of 2 × 960 samples, providing the network with sufficient temporal context to capture the structural hysteresis and inertial effects.

The training loss in Figure 9 shows a clear downward trend and eventually stabilizing below 0.1 MSE. This indicates that the model is successfully learning from the training data and on the other hand, the plateau towards the end of the epochs suggests the model has reached its learning capacity for the given architecture and parameters. Regarding the presence of some oscillations and spikes—potentially due to a high learning rate or complex data features—particularly around iteration 50 and periodically thereafter (e.g., iterations 140, 200, 280), the variance health remains robust, and the optimizer recovers after each spike and continues to decrease the loss.

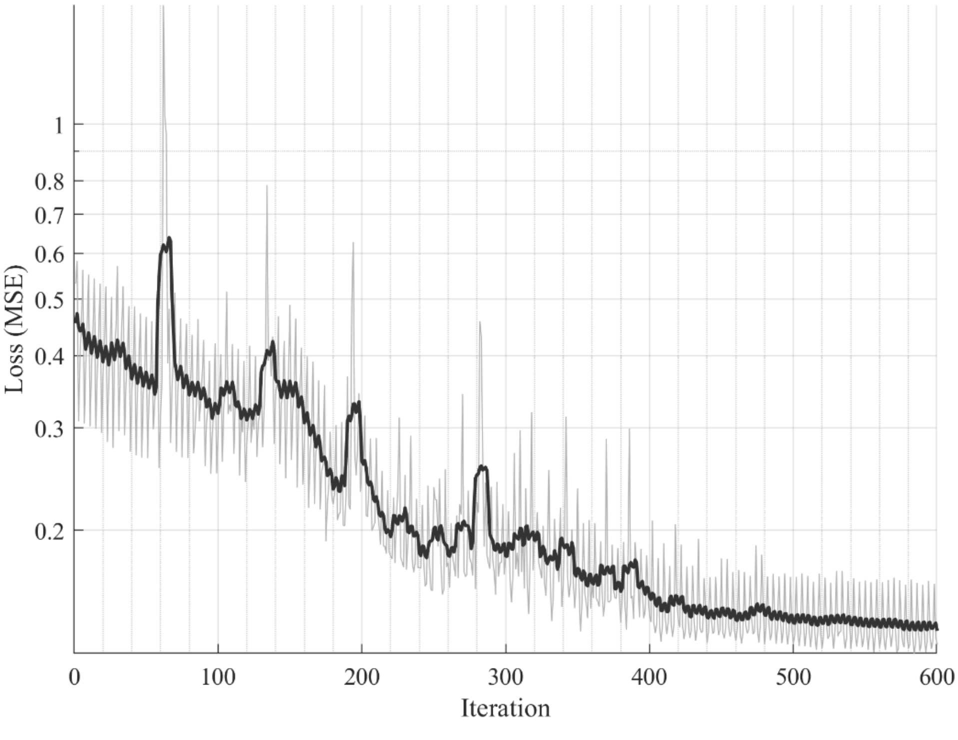

Figure 9. Training loss along the first 600 iterations.

The results of the training process are presented in Table 4; the training of the model has been based on optimizing RMSE. Maximum RMSE is 7.8 mm for the last phase. Apparently, RMSE increases with shaking intensity. Correlation R is higher than 90% for the training phases and SNR is below 10 dB. The validation phase (at nominal PGA = 0.20 g) shows performance with R close to 80% similar to R attained in other cases e.g., [40] and peak-to-peak error ε_{peak} = 16% (Figure 10).

Table 4. Evaluation metrics for LSTM model.

Set	PGA (g%)	Correlation (R)	RMSE (mm)	ε_{peak} (%)	SNR (dB)
Training	5	0.94	0.91	0.7	9.0
Training	10	0.91	2.21	8.5	7.4
Validation	20	0.80	7.10	15.8	4.4
Training	30	0.93	5.61	2.8	8.7
Training	40	0.94	7.76	5.3	9.3

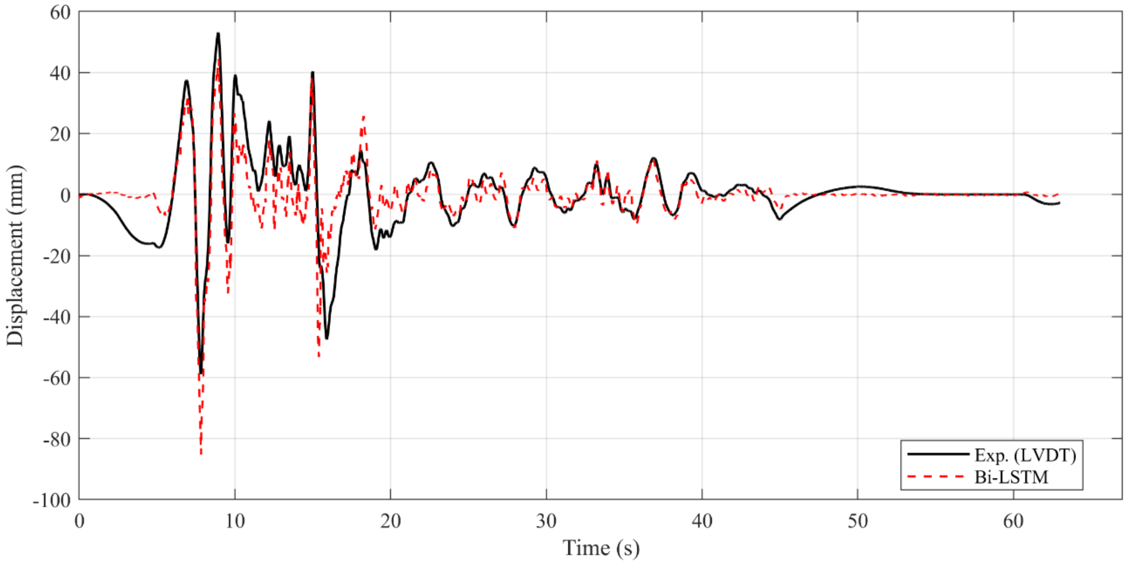

Figure 10. Comparison of the recorded displacement (LVDT) and the data-driven model (LSTM) for test phase 3 (validation) at nominal PGA = 0.20 g.

To further investigate the performance drop in Phase 3 (0.20 g), we conducted a sensitivity analysis by rotating the validation set to Phase 2 (0.10 g). The results remained consistent (Validation R = 0.78; Training R = [0.94; 0.90; 0.94; 0.94]). This indicates that the performance gap is not specifically tied to structural nonlinearity at 0.20 g, but rather reflects the inherent challenge of seismic signal reconstruction for 'unseen' records. The consistency of these results across different validation splits confirms the model's stability and its ability to provide a reliable 'lower bound' of R ≈ 0.80 for blind displacement reconstruction.

5.2. Convolutional Bidirectional Long-Short Term Memory Neural Network (CNN-BiLSTM)

In this approach lightly filtered input is used in the ML modelling. We use band-pass FIR filters in the time domain with cut-off frequencies ω_{hp} = 0.1 Hz and pass frequency ω_{lp} = 50 Hz far enough from the modal frequencies of the building. The ML architecture follows the same structure.

The results are presented in Table 5 where similar pearson correlation factors R are observed but higher RMSE and ε_{peak} errors are obtained. In Figure 11, the reconstructed displacements versus the recorded ones for validation phase 3 (at nominal PGA = 0.20 g) are shown.

Table 5. Evaluation metrics for LSTM model with filtered input.

PGA (g%)	Correlation (R)	RMSE (mm)	ε_{peak} (%)
5	0.93	0.94	7.5
10	0.91	2.20	8.4
20	0.84	6.29	40.6
30	0.93	5.69	6.2
40	0.93	8.08	4.6

The performance divergence observed at the 0.20 g validation phase (R = 0.84) highlights the challenge of real-time structural state estimation during the onset of nonlinearity. Unlike the NC optimum filter, which benefits from global signal knowledge to eliminate phase lag, the causal LSTM architecture must balance a trade-off between temporal latency and reconstruction accuracy, particularly as cumulative errors in the recurrent units become more pronounced during long-duration seismic excitation.

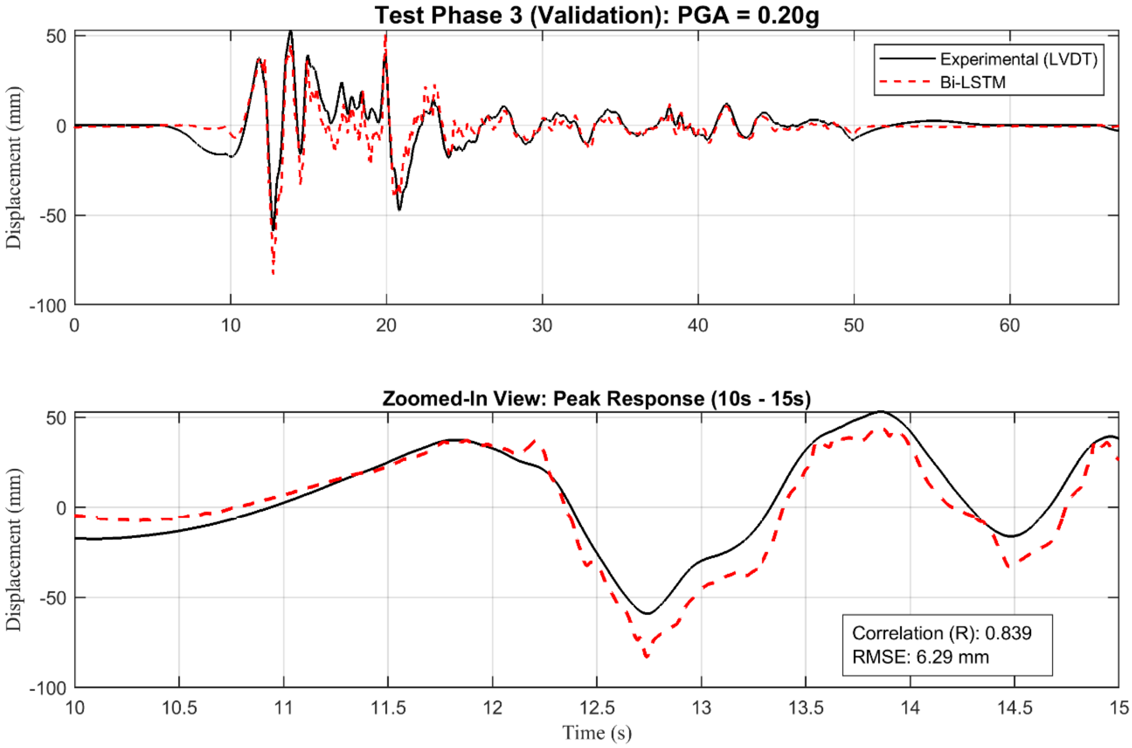

Figure 11. Comparison between predicted and measured by LVDT displacement response.

6. Comparison and Discussion

The comparison of the evaluation metrics of the four methods applied is presented in Figure 12. Based on the evaluation metrics provided, the NC (optimized) model consistently outperforms the other techniques across all seismic test phases. In the Correlation (R) analysis, the NC model achieves the highest values, particularly in Phase 4 where it reaches near 0.99, while the LSTM (filter) and standard LSTM show significantly lower performance in earlier phases. A similar trend is evident in the SNR (dB) metric, where the NC model (purple) maintains a clear lead, suppressing above 15 dB in Phase 4, whereas the Adaptive model (yellow) and standard LSTM follow in descending order of denoising. Conversely, the RMSE (mm) and ε_p error (%) plots demonstrate that the NC model minimizes prediction inaccuracies most effectively, showing the lowest bars across nearly all phases. While the Adaptive model remains a competitive second-best, the LSTM variants exhibit higher error margins and lower signal-to-noise ratios, confirming that the NC approach provides the most accurate structural displacement reconstruction.

However, it should be highlighted that the decomposition of the signal in the frequency domain is carried out using periodic functions extending to infinity. This imposes some assumptions to the conversion introducing some uncertainty regarding the representation as in most cases the signal comes from a nonlinear system. On the contrary, this is not a constraint for the time domain where periodicity is not a prerequisite and not for the data-driven model. Therefore, the latter methods from the theoretical point of view have an advantage when the structural behavior is nonlinear (phases 3 to 5). However, for the linear range of the structural response (phase 1 to 2) the SNR is relatively low and thus, the application of digital causal filters should be performed with increased caution. As an alternative an adaptive modelling procedure is proposed which tries to imitate the efficiency of the former methods.

The comparative assessment of the Adaptive Wiener Filter and the NC ideal filter does not support a universal conclusion. The NC filter suppresses everything outside the cut-off frequencies, regardless of whether that energy is noise or real structural signal. On the other hand, the adaptive filter looks at the statistical correlation. If there is a specific noise frequency (e.g., a mechanical resonance from the shaking table’s pump), the adaptive filter can “target” and suppress that specific noise while trying to preserve potential nearby structural frequencies. Therefore, the adaptive filter can drive to a “smoother” acceleration trace than the ideal filter, which can make the integration to velocity less erratic. Moreover, the adaptive filter is mathematically designed to maximize the SNR whereas, NC ideal filter simply limits the bandwidth. However, the NC ideal filter has zero phase shift ensuring that peaks align perfectly in time with the peaks of the displacement. The adaptive filter is a standard causal FIR filter which introduces a time delay. Even a small delay of a few milliseconds can significantly drop the correlation (R) and increase the RMSE when compared to the LVDT.

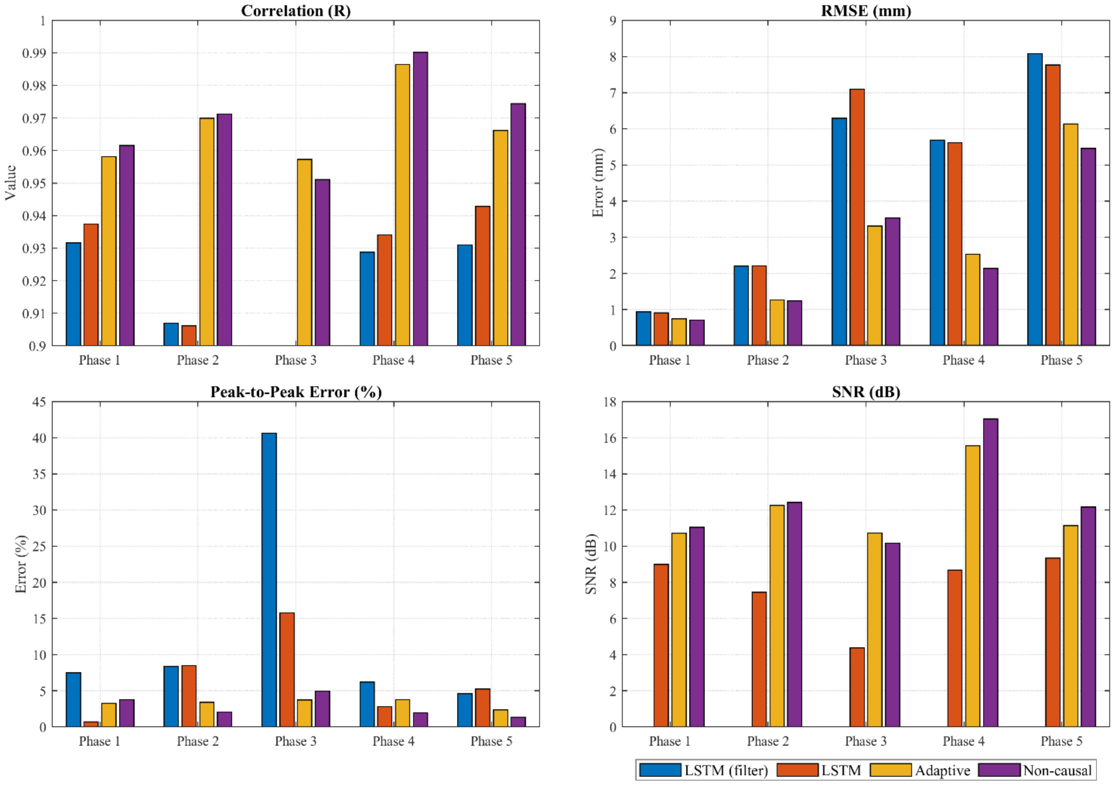

Figure 12. Comparison of the evaluation metrics for the methods applied.

The recurrent layers of the Bi-LSTM function as learned numerical integrators, where the internal gating mechanisms regulate the accumulation of acceleration data into displacement estimates. This implicit approximation allows the model to map the input-output relationship of the masonry wall while simultaneously suppressing the low-frequency noise that typically destabilizes standard discrete integration methods. However, there exist a performance gap between the LSTM and the NC optimum filter which highlights the inherent challenges of approximating these operators in a causal framework without 'future' context to bound integration drift.

7. Conclusions

This study evaluated signal processing and deep learning methodologies for reconstructing reliable displacement traces from the seismic response of a full-scale, two-story unreinforced stone masonry building using recorded data from a shaking table test. While acceleration data is readily available, the double integration required to retrieve displacement is highly susceptible to noise-induced drift.

Advanced filtering techniques have been applied employing non-causal (NC) ideal filters and adaptive (causal) filters. To effectively suppress noise the cut-off frequencies were selected after optimization. The comparison of the obtained displacement time-histories to the one measured by displacement transducers showed that very high correlations can be achieved and reliable estimates of displacements can be made. The denoising carried out in the frequency domain with a non-causal filter was, however, more accurate than the adaptive FIR filter.

To overcome the rigidities of traditional filtering, a stacked Long Short-Term Memory (LSTM) recurrent neural network was implemented. By training on a range of seismic intensities (0.5–0.40 g) and optimizing hyperparameters (Learning Rate, L2 Regularization, and Dropout) via Bayesian Optimization, the following was observed:

- Implicit Denoising: The 256/128-unit, 2-layer LSTM architecture successfully learned the integration physics while implicitly performing baseline correction, eliminating the need for manual filter selection achieving reliable results and generalizing sufficiently well.
- Nonlinear Robustness: The RNN performed better during the high-intensity PGAs 0.3 g and 0.40 g phase, where it effectively mapped the complex, nonlinear relationships between acceleration and displacement that usually cause mathematical drift.

- Validation: Validation on the intermediate 0.20 g record confirmed the model's ability to interpolate structural behavior across different seismic demand levels.
- Deep learning approaches provide a viable complementary methodology, particularly for complex nonlinear systems and automated structural monitoring applications.

The inclusion of an NC 'optimum' benchmark serves as a theoretical upper bound for reconstruction accuracy, allowing for a quantitative assessment of the performance trade-offs inherent in real-time causal architectures. By comparing the proposed Bi-LSTM against this NC reference, we demonstrate the model's ability to minimize the phase lag and drift errors typically associated with real-time seismic signal processing.

Author Contributions

L.A.K.: conceptualization, methodology, data curation, visualization, writing—original draft preparation, A.P. and G.D.: funding acquisition, supervision and writing—reviewing and editing. All authors have read and agreed to the published version of the manuscript.

Institutional Review Board Statement

Not applicable.

Informed Consent Statement

Not applicable.

Funding

The financial support provided by Istituto Universitario di Studi Superiori (doctoral cycle XXIV), Italian Civil Protection (research project C.2.1.2 of EUCENTRE (Pavia, Italy)) and the Department of Civil and Architectural Engineering (research project 'Analysis of the experimental response of shake table tests' n. 416/16.3.201) is gratefully acknowledged for carrying out this research.

Data Availability Statement

The raw and processed data and model results generated during the current study are available from the corresponding author on reasonable request and subject to permission from EUCENTRE.

Acknowledgments

The kind suggestions and recommendations of Pietro Savazzi from the University of Pavia for adaptive filters are highly appreciated.

Conflicts of Interest

The authors declare no conflict of interest.

Use of AI and AI-Assisted Technologies

During the preparation of this work, the authors used Gemini to debug the code and proofread the text. After using this tool/service, the authors reviewed and edited the content as needed and take full responsibility for the content of the published article.

References

1. Severn, R.T. The development of shaking tables-A historical note. *Earthq. Eng. Struct. Dyn.* **2011**, *40*, 195–213. https://doi.org/10.1002/eqe.1015.
2. Stiros, S.C. Errors in velocities and displacements deduced from accelerographs: An approach based on the theory of error propagation. *Soil Dyn. Earthq. Eng.* **2008**, *28*, 415–420. https://doi.org/10.1016/j.soildyn.2007.07.004.
3. Strobbia, C.; Zarkhidze, A.; May, R.; et al. Model-based attenuation for scattered dispersive waves. *Geophys. Prospect.* **2014**, *62*, 1143–1161. https://doi.org/10.1111/1365-2478.12118.
4. Boore, D.M.; Bommer, J.J. Processing of strong-motion accelerograms: Needs, options and consequences. *Soil Dyn. Earthq. Eng.* **2005**, *25*, 93–115. https://doi.org/10.1016/j.soildyn.2004.10.007.

5. Smerzini, C.; Galasso, C.; Iervolino, I.; et al. Ground Motion Record Selection Based on Broadband Spectral Compatibility. *Earthq. Spectra* **2014**, *30*, 1427–1448. https://doi.org/10.1193/052312EQS197M.
6. Thong, Y.K.; Woolfson, M.S.; Crowe, J.A.; et al. Numerical double integration of acceleration measurements in noise. *Measurement* **2004**, *36*, 73–92. https://doi.org/10.1016/j.measurement.2004.04.005.
7. Zheng, W.; Dan, D.; Cheng, W.; et al. Real-time dynamic displacement monitoring with double integration of acceleration based on recursive least squares method. *Measurement* **2019**, *141*, 460–471. https://doi.org/10.1016/j.measurement.2019.04.053.
8. Pan, C.; Zhang, R.; Luo, H.; et al. Baseline correction of vibration acceleration signals with inconsistent initial velocity and displacement. *Adv. Mech. Eng.* **2016**, *8*, 1–11. https://doi.org/10.1177/1687814016675534.
9. Chen, Z.; Fu, J.; Peng, Y.; et al. Baseline Correction of Acceleration Data Based on a Hybrid EMD–DNN Method. *Sensors* **2021**, *21*, 6283. https://doi.org/10.3390/s21186283.
10. Chen, T.; Son, Y.J.; Park, A.; et al. Baseline correction using a deep-learning model combining ResNet and UNet. *Analyst* **2022**, *147*, 4285–4292. https://doi.org/10.1039/d2an00868h.
11. Gillet, L.C.; Guo, X.; Liu, M.; et al. Deep learning baseline correction method via multi-scale analysis and regression. *Chemom. Intell. Lab. Syst.* **2023**, *235*, 104779. https://doi.org/10.1016/j.chemolab.2023.104779.
12. Drosopoulos, G.A.; Stavroulakis, G.E. DeepONet for the Prediction of Failure Response of a Two-Dimensional Fibre-Reinforced Composite Plate. *Bull. Comput. Intell.* **2025**, *1*, 76–88. https://doi.org/10.53941/bci.2025.100005.
13. Khatti, J.; Kontoni, D.-P. N. Assessment of Bearing Capacity of Concrete Piles in Alluvial Soils Using Bio and Swarm-Optimized Artificial Neural Network Models. *Bull. Comput. Intell.* **2025**, *1*, 53–75. https://doi.org/10.53941/BCI.2025.100004.
14. Bardhan, A.; Kardani, N. An Efficient Meta-Ensemble Paradigm for Modelling Poisson’s Ratio and Maximum Horizontal Stress in Casing Collapse Hazard. *Bull. Comput. Intell.* **2026**, *2*, 146–163. https://doi.org/10.53941/BCI.2026.100008.
15. Ghorbanzadeh, S.; Daei, A.; Armaghani, D.J.; et al. On the interpretability of machine and deep learning techniques for predicting CBR of stabilized soil containing agro-industrial wastes. *Sci. Rep.* **2026**, *16*, 1570. https://doi.org/10.1038/s41598-025-30501-8.
16. Afrazi, M.; Jahed Armaghani, D.; Afrazi, H.; et al. Real-time monitoring of tunnel structures using digital twin and artificial intelligence: A short overview. *Deep Undergr. Sci. Eng.* **2025**. https://doi.org/10.1002/DUG2.70029.
17. Newland, D.E. *An Introduction to Random Vibrations, Spectral & Wavelet Analysis*; Dover Publications: Garden City, NY, USA, 2012.
18. Inman, D.J. *Engineering Vibration*, 3rd ed.; Pearson Education, Inc.: Hoboken, NJ, USA, 2001.
19. Calvi, G.M.; Pavese, A.; Ceresa, P.; et al. *Design of a Large-Scale Dynamic and Pseudo-Dynamic Testing Facility*; IUSS Press: Rome, Italy, 2005.
20. Magenes, G.; Penna, A.; Galasco, A. A Full-Scale Shaking Table Test on a Two-Storey Stone Masonry Building. In Proceedings of the 14th European Conference on Earthquake Engineering, Ohrid, FYROM, 30 August–3 September 2010.
21. Magenes, G.; Penna, A.; Senaldi, I.E.; et al. Shaking Table Test of a Strengthened Full-Scale Stone Masonry Building with Flexible Diaphragms. *Int. J. Archit. Herit.* **2014**, *8*, 349–375. https://doi.org/10.1080/15583058.2013.826299.
22. Kouris, L.A.S.; Penna, A.; Magenes, G. Assessment of a Full-Scale Unreinforced Stone Masonry Building Tested on a Shaking Table by Inverse Engineering. *Buildings* **2022**, *12*, 1235. https://doi.org/10.3390/buildings12081235.
23. Kouris, L.A.S.; Penna, A.; Magenes, G. Seismic damage diagnosis of a masonry building using short-term damping measurements. *J. Sound Vib.* **2017**, *394*, 366–391. https://doi.org/10.1016/j.jsv.2017.02.001.
24. Kouris, L.A.S.; Penna, A.; Magenes, G. Dynamic Modification and Damage Propagation of a Two-Storey Full-Scale Masonry Building. *Adv. Civ. Eng.* **2019**, *2019*, 2396452. https://doi.org/10.1155/2019/2396452.
25. Zhou, Z.; Liu, G.; Bai, M.; et al. Patch selection-based dual attention unsupervised deep learning model for suppressing random and erratic noise in seismic data. *J. Appl. Geophys.* **2026**, *246*, 106107. https://doi.org/10.1016/j.jappgeo.2026.106107.
26. Akeila, E.; Salcic, Z.; Swain, A. A self-resetting method for reducing error accumulation in INS-based tracking. In *IEEE/ION Position, Location and Navigation Symposium*; IEEE, 2010; pp 418–427. https://doi.org/10.1109/PLANS.2010.5507179.
27. Thong, Y.K.; Woolfson, M.S.; Crowe, J.A.; et al. Dependence of inertial measurements of distance on accelerometer noise. *Meas. Sci. Technol.* **2002**, *13*, 1163–1172. https://doi.org/10.1088/0957-0233/13/8/301.
28. Zhu, Y. An Accurate Calculation Method of Vibration Displacement Based on Vibration Acceleration Signal. *J. Inf. Comput. Sci.* **2015**, *12*, 41–49. https://doi.org/10.12733/jics20104848.
29. Massa, M.; Pacor, F.; Luzi, L.; et al. The ITalian ACcelerometric Archive (ITACA): Processing of strong-motion data. *Bull. Earthq. Eng.* **2010**, *8*, 1175–1187. https://doi.org/10.1007/s10518-009-9152-3.
30. Pacor, F.; Paolucci, R.; Ameri, G.; et al. Italian strong motion records in ITACA: Overview and record processing. *Bull. Earthq. Eng.* **2011**, *9*, 1741–1759. https://doi.org/10.1007/s10518-011-9295-x.
31. Ciarella, S.; Trinquier, J.; Weigt, M.; et al. Machine-learning-assisted Monte Carlo fails at sampling computationally hard problems. *Mach. Learn. Sci. Technol.* **2023**, *4*, 010501. https://doi.org/10.1088/2632-2153/acbe91.
32. Clarke, G.K.C. Optimum second-derivative and downward continuation filters. *Geophysics* **1969**, *34*, 424–437.

33. Zeng, X.; Li, X.; Jia, W.; et al. Iterative Wiener filter for unstable linear transformations of potential field data. *J. Appl. Geophys.* **2015**, *115*, 100–109. https://doi.org/10.1016/j.jappgeo.2015.02.006.
34. Trompat, H.; Boschetti, F.; Hornby, P. Improved downward continuation of potential field data. *Explor. Geophys.* **2003**, *34*, 249–256. https://doi.org/10.1071/EG03249.
35. Gunn, P.J. Application of Wiener filters to transformations of gravity and magnetic fields. *Geophys. Prospect.* **1972**, *20*, 860–871.
36. Zeng, X.; Liu, D.; Li, X.; et al. An improved regularized downward continuation of potential field data. *J. Appl. Geophys.* **2014**, *106*, 114–118. https://doi.org/10.1016/j.jappgeo.2014.04.015.
37. Lai, C.-A. NLMS algorithm with decreasing step size for adaptive IIR filters. *Signal Process.* **2002**, *82*, 1305–1316. https://doi.org/10.1016/S0165-1684(02)00275-X.
38. Wang, W.; Gu, Z.; Song, Q.; et al. U-Net3+ with full-scale fusion and deep supervision for seismic noise suppression. *J. Appl. Geophys.* **2026**, *247*, 106122. https://doi.org/10.1016/j.jappgeo.2026.106122.
39. Xu, W.; Lipari, V.; Bestagini, P.; et al. Self-Supervised Seismic Swell Noise Suppression from Noisy Seismic Data. *IEEE Trans. Geosci. Remote Sens.* **2024**, *62*, 5935813. https://doi.org/10.1109/TGRS.2024.3497163.
40. Shen, J.; Zhang, L.; Zhu, B. Prediction of Structural Displacement from Acceleration Based on Improved Long Short-Term Memory Networks. *Struct. Control Health Monit.* **2025**, *2025*, 2290381. https://doi.org/10.1155/stc/2290381.